AGU PUBLICATIONS

Geophysical Research Letters

RESEARCH LETTER

10.1002/2016GL071304

Time reversal imaging of the 2015 Illapel tsunami source

Chao An[1] and Lingsen Meng[1]

[1]Earth, Planetary, and Space Sciences, UCLA, Los Angeles, California, USA

Key Points:

- We applied the time reversal imaging technique to the 2015 *M*8.3 Illapel event to image the tsunami source
- Albeit limited by the azimuth coverage of tsunami stations, we produce a reasonable image of the tsunami source using four stations
- Results show an initial water elevation profile with maximum height of 2.0 m located 30 km from trench, indicating little near-trench slip

Supporting Information:

- Supporting Information S1

Correspondence to:
L. Meng,
meng@epss.ucla.edu

Citation:
An, C., and L. Meng (2017), Time reversal imaging of the 2015 Illapel tsunami source, *Geophys. Res. Lett.*, *44*, 1732–1739, doi:10.1002/2016GL071304.

Received 21 SEP 2016
Accepted 20 JAN 2017
Accepted article online 27 JAN 2017
Published online 22 FEB 2017

©2017. American Geophysical Union.
All Rights Reserved.

Abstract Studies of the 2015 Illapel earthquake show large variance in the east-west location of the principal slip, and it is also controversial if there is significant slip near the trench. In this study, we derive the initial water elevation from tsunami waves based on the time reversal imaging technique. This approach does not make assumptions on the fault geometry required by finite-fault inversions. We adopt 4 out of total 24 stations based on their azimuthal coverage in the time reversal analysis. Additionally, we introduce a correction that scales the wave amplitude at each station by the epicentral distance to account for the 2-D spreading effects. The results show a focused region of water elevation with a maximum height of 2.0 m located approximately 30 km from the trench. By comparison to the initial deformation predicted by several finite-fault models, our results indicate minimum slip distribution near the trench.

1. Introduction

The technique of time reversal (TR) imaging was first developed in acoustic experiments [*Fink*, 1992; *Fink et al.*, 2000; *Tanter et al.*, 2000]. In a typical TR experiment, arrays of transducers time reverse the sound they receive and send it back to the original source as if the process of wave propagation was reversed in time. The sound then refocuses near the source and recovers the originally transmitted signal. The technique is valid based on the reciprocity principle that applies to standard wave equations. In recent years, efforts have been devoted to exploring the TR of seismic recordings to image the earthquake rupture processes [e.g., *Larmat et al.*, 2006; *Kawakatsu and Montagner*, 2008]. The TR technique is more applicable to tsunami waves because they can be accurately simulated given well-known bathymetry.

The first application of the TR technique to a real tsunami event was conducted by *Hossen et al.* [2015a]. Recordings from various tsunami sensors were adopted to establish the initial sea displacement of the tsunami generated by the 2011 *M*9.0 Tohoku earthquake. It was found that the reduction in the number of stations from 17 to 12 did not affect the refocused image. However, a good azimuth coverage is necessary to recover the tsunami source. *Hossen et al.* [2015a] also conducted tests of two different approaches of weighting — uniform scaling and station-dependent weighting. In the first approach, the TR image was scaled to match the maximum recorded wave height at each station in a least squares sense. In the second approach, each TR image from an individual station was scaled based on the reduction of wave amplitude during the forward and reverse propagation, and all the separate TR images were averaged to construct the final TR image. *Hossen et al.* [2015a] showed that the two approaches led to similar initial elevation profiles, in terms of area and peak height, but the forward predicted waveforms using the refocused sources better matched the observations for uniform scaling. In their later work, *Hossen et al.* [2015b] attempted to account for the water depth variance in the source region. To accomplish this, every individual TR image was corrected by the Green's functions from the source grids to receiver stations. The results showed that the final image could accurately predict the tsunami waveforms at local and far-field distances, and they therefore suggested that the technique has the potential to provide tsunami warnings in a real event. Although in *Hossen et al.* [2015b], the Green's function from a source grid to an observation station was taken to be the same as that from the station to the source, the two Green's functions must be different by a factor of the water depth ratio. TR analysis involves no assumptions about the fault geometry and also excludes the trade-off of smoothing factors that are required by finite-fault inversions [*Satake*, 1987; *Fujii et al.*, 2011; *Satake et al.*, 2013; *Wei et al.*, 2013; *An et al.*, 2014; *Lay et al.*, 2014; *Yagi et al.*, 2014; *Gusman et al.*, 2015; *Heidarzadeh et al.*, 2016a] and inversions of initial water elevation [*Baba et al.*, 2005; *Tsushima et al.*, 2011, 2014]. Therefore, it is useful to recover the tsunami source solely from tsunami data, especially to detect nonseismic components of tsunami sources [*Hossen et al.*, 2015a]. On the other hand, lacking other constraints also means that the choice of weighting

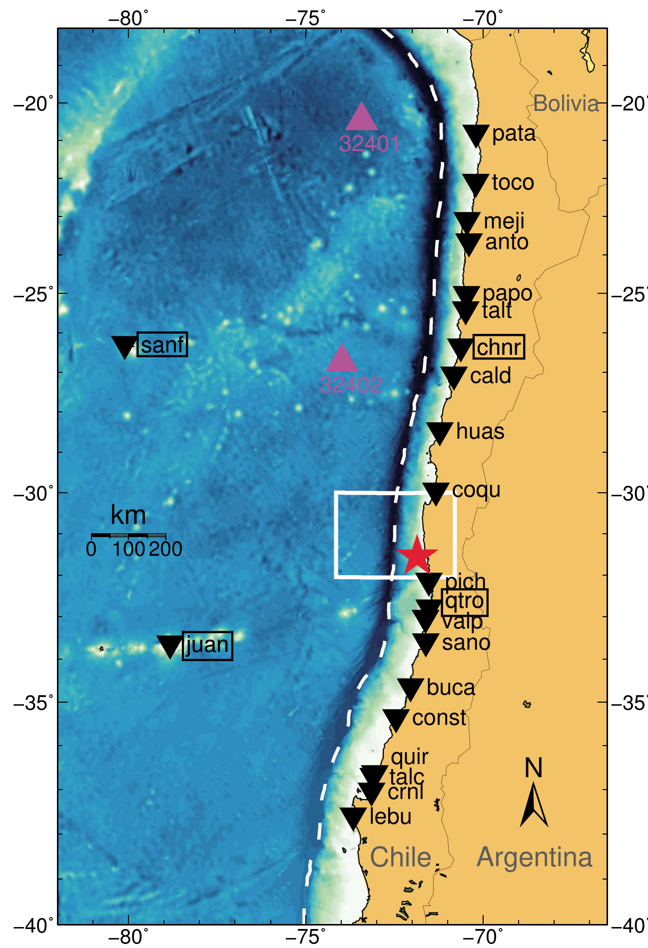

Figure 1. The location of tsunami stations in the 2015 Illapel event. The red star shows the earthquake epicenter (71.864°W, 31.553°S) given by Centro Sismológico Nacional (Chile) (CSN), black inverted triangles mark the tide gauges, and magenta triangles denote the DART stations. Stations with framed boxes around their names are adopted in the TR analysis. The tide gauges are identified as follows: pich(Pichidangui), qtro(Quintero), valp(Valparaiso), sano(San Antonio), buca(Bucalemu), const(Constitucion), quir(Quiriquina), talc(Talcahuano), crnl(Coronel), lebu(Lebu), coqu(Coquimbo), huas(Huasco), cald(Caldera), chnr(Chañaral), talt(Taltal), papo(Paposo), anto(Antofagasta), meji(Mejillones), toco(Tocopilla), pata(Patache), juan(Juan Fernandez), and sanf(San Felix). The computational domain in the TR analysis is the same as shown in this figure. The white box identifies the region of tsunami source shown in Figure 2.

factors for each station plays an important role in TR analysis. In this study, we introduce a new approach of weighting based on the 2-D spreading effects of water waves.

On 16 September 2015 22:54:33 UTC, a M_w 8.3 earthquake occurred near Illapel, Chile, generating a tsunami wave with maximum runup of 11 m [e.g., *Fuentes et al.*, 2016]. The tsunami waves were recorded by more than 20 tsunami stations. However, most of these stations are located along the coastline that is parallel to the strike direction of the fault, with the exception of only two DART (Deep-ocean Assessment and Reporting of Tsunamis) stations in the open ocean and two tide gauges on islands in the eastern Pacific (Figure 1). Thus, the azimuthal coverage of the stations is far from ideal, and the ability to apply TR analysis to this event is questionable. In addition, it was found that the near-trench portion of a subduction zone was capable of holding huge coseismic slip and generating megatsunamis [e.g., *Kanamori*, 1972; *Maeda et al.*, 2011; *Sato et al.*, 2011; *Fujii et al.*, 2011; *Lay et al.*, 2011; *Shao et al.*, 2011; *Yue and Lay*, 2011; *Satake et al.*, 2013], so it is obvious societal importance for characterizing tsunami hazards to understand if significant slip occurs in a subduction earthquake [e.g., *Lay et al.*, 2012; *Ma*, 2012; *Yue et al.*, 2014]. However, mixing results were obtained about whether the rupture reached the trench during the Illapel event. For instance, *Melgar et al.* [2016] jointly inverted high-rate GPS records, strong motion records, interferometric synthetic aperture radar (InSAR), and tsunami records and concluded that the slip was segmented into two domains, with the shallow slip patch rupturing all the way to the trench. *Li et al.* [2016] performed iterative modeling of teleseismic body waves and tsunami waves and also found the rupture extending to the trench. *Tilmann et al.* [2016] jointly inverted seismic, strong motion, GPS, and InSAR data and derived slip of 4.7 m near the trench. On the other hand, *Heidarzadeh et al.* [2016b] preferred the slip concentrated in a large area between the trench and coastline based on finite-fault inversions of teleseismic data and forward simulations of tsunami waves. In this study, we derive the initial water elevation profile based on the TR technique four tsunami stations located at different azimuths, which is then compared with the sea surface deformation predicted by finite-fault models. Such comparison allows us to infer the location and extent of the principal slip of the 2015 Illapel earthquake.

2. Data and Method

The 22 tide gauges and two nearby DART stations that recorded the tsunami waves in the 2015 Illapel event are shown in Figure 1. All the tide gauges are located along the nearly straight north-south trending coastline except juan and sanf (the full names of the stations are given in the caption of Figure 1). We adopt observations from four stations, qtro, chnr, juan and sanf, in the TR process, which are selected based on the azimuthal coverage. First, juan and sanf are chosen since they are the only two with a relatively large oblique angle to the fault strike (>30°). Then, two more stations are selected to the north and south of the epicenter. Tests of trial and error show that the choice in the north has little impact on the results, so chnr is chosen with its epicentral distance comparable to juan and san. In the south, tests show that station qtro generates less artifacts along the coastline than other southern stations.

The length of tsunami data implemented in the TR analysis is 12,000 s for all stations. First, all the records are truncated to keep only the leading crest. This corresponds to the wave propagation from the tsunami source directly to observation stations with little interaction with the coastline. This part of the tsunami wave can be accurately simulated by linear shallow water wave equations. The truncated signals are then padded with zeros up to the full time length, reversed in time, and then implemented as source terms at the observation stations in tsunami simulation. Waves from those sources propagate from stations to the source and interfere with each other to recover the tsunami source. Following the reciprocity principle for tsunami waves [*Korolev*, 2011; *Hossen et al.*, 2015a], each tsunami source has a cylindrical shape. The radius of the cylinder is $t_0\sqrt{gh}$, where $t_0 = 10$ s, g is the gravitational acceleration, and h is the water depth at the observation station. The height of the cylinder is forced to vary as the time-reversed realistic recordings at the station. In our analysis, we perform the TR simulation for each tsunami station separately and then sum up all the TR images from individual stations to construct the final TR image. The TR results from other combinations of stations can thus be easily obtained without recalculations. The TR image after summation is linearly scaled by the maximum amplitude of all the 24 stations to generate the final TR image. The whole process is equivalent to a simultaneous TR simulation of all the used stations as it is a linear system. The linear version of COMCOT, a tsunami simulation package [*Liu et al.*, 1998; *Wang and Liu*, 2006, 2007; *An et al.*, 2014], is adopted to compute the tsunami waveforms. The bathymetry resolution is 30 arc sec extracted from the General Bathymetric Chart of the Oceans (GEBCO_2014) bathymetry data, and the time step is 1.0 s to satisfy the C.F.L. condition. In the numerical simulations, the locations of the tide gauges are shifted up to a few kilometers toward the ocean in order for them to be located in the water [e.g., *Gusman et al.*, 2015]. Wave nonlinearity is negligible at DART stations because the ratio of wave amplitude and water depth is very small [e.g., *An and Liu*, 2014]. A list of the water depth at the tide gauges is given in the supporting information (Table S2). *Shuto* [1991] suggests that linearity holds for water depth more than 50 m, so nonlinearity could be significant for tide gauges in shallow water. Nevertheless, recent simulations of the 2014 Iquique tsunami using local bathymetry of high resolution show that the overall nonlinearity is small for most of the tide gauges [*An et al.*, 2014]. We therefore choose to neglect wave nonlinearity in this study.

In the analysis, it is found that the amplitude decay due to the 2-D spreading effects varies because of the difference in the distance from the tsunami source to the observation stations. For example, the distance from the four used stations, qtro, chnr, juan and sanf, to the Centro Sismológico Nacional (Chile) (CSN) epicenter (71.864°W, 31.553°S) is 139.2 km, 591.0 km, 691.2 km, and 993.1 km, respectively, causing differences in wave amplitude decay. Based on shallow water wave equations, the wave amplitude decays as $\sqrt{r}$ with distance [e.g., *Kajiura*, 1963], where r is the distance from the source to an observation point. Obviously, tsunami stations located farther from the source record smaller waves and in the TR process the waves become even smaller after propagating from station to the source. Station qtro is the closest station to the epicenter among the four used stations, so the wave amplitude at qtro, as well as the amplitude of TR image obtained from

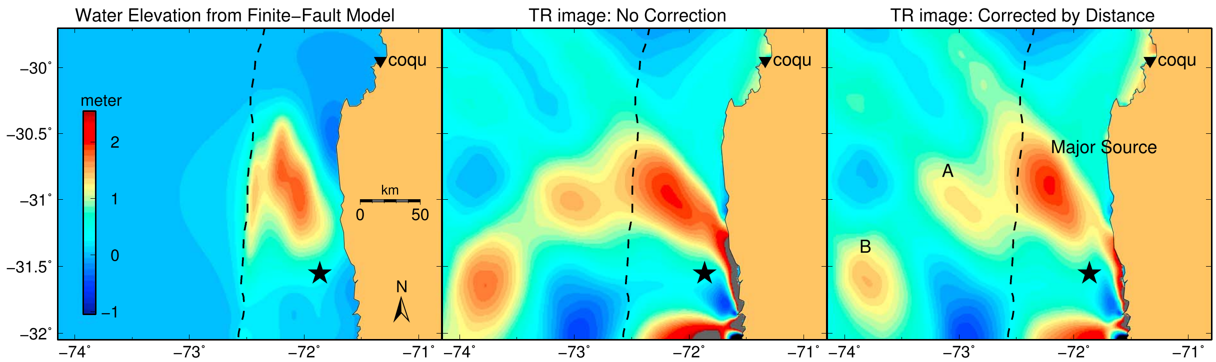

Figure 2. The TR image of the 2015 Illapel tsunami source. (left) Initial water elevation inferred from a finite-fault inversion of tsunami, InSAR, and GPS data. (middle and right) The display of the TR images with and without distance correction. In Figure 2 (right), each individual TR image from the four stations is multiplied by a correction factor (given in Table S3 in the supporting information), summed up, and then scaled to match the maximum wave amplitude at all the 24 stations in a least squares sense. In Figure 2 (middle), the four individual TR images are summed up directly and then scaled to be same maximum wave height in the source as Figure 2 (right). The black star marks the CSN epicenter, and the black dashed line denotes the trench.

qtro, is much larger than the other three stations. So the final TR image is dominated by the individual TR image from station qtro. Thus, it is necessary to correct the wave amplitude to account for the 2-D spreading effects. In our TR analysis, the wave amplitude at each station is multiplied by a factor of $\sqrt{2r}$ to eliminate the amplitude decay due to 2-D spreading. The distance is chosen to be $2r$ instead of r to account for the wave propagation from the source to the station and the reverse propagation from the station to the source. Apart from the spreading decay, the wave amplitude is also affected by the water depth, i.e., waves propagating to shallow water will reduce wavelength and increase amplitude. For example, DART 32402 with water depth of 4070.0 m recorded a wave height of ~0.12 m, but tide gauge chnr with water depth of 24.0 m recorded ~0.43 m, although their epicentral distance and azimuth are close. However, this effect is also reversed in the reverse propagation, so waves propagating from 32402 to the source gets amplified by entering shallower water, but waves from chnr become smaller due to increase of water depth. Thus, the effects of water depth variation are automatically taken in account in the TR simulations. A synthetic example is displayed in the supporting information (Figure S1), which shows that the original, final TR image is dominated by the TR image from the closest station but with the correction by $\sqrt{2r}$, the images from other stations become stronger and the final image is significantly improved. In our TR analysis for the Illapel event, we use the distance along the great circle path from a station to the CSN epicenter to perform the amplitude correction. A list of the amplitude correction for all the stations is given in Table S3 in the supporting information.

3. Results

The initial sea surface elevation in the 2015 Illapel earthquake obtained from the TR analysis is shown in Figure 2. The initial water deformation predicted by a finite-fault model based on joint inversion of the tsunami, InSAR, and GPS data is plotted in Figure 2 (left). This model is hereinafter referred to as our finite-fault model. The details of the inversion are provided in the supporting information (Text S1 and Figures S3–S5) [*Okada*, 1985]. Figure 2 (middle and right) displays the TR images with and without distance correction of 2-D spreading, respectively. Both the two TR images show a focused source of water elevation located about 30 km to the east of the trench and about 70 km to the northwest of the CSN epicenter. This is very similar to that obtained from our finite-fault model. The maximum water height obtained by TR imaging is ~2.0 m, which is very close to that from joint inversion (~1.8 m). Figure 2 (middle and right) compares the TR images before and after the correction. It is clear that the correction enhances the major tsunami source from the wave focusing near the coastline. The correction also weakens the artifacts to the southwest, leading to a more focused tsunami source image.

The TR images also show two areas of artifacts to the southwest of the major tsunami source (A and B in Figure 2), owing to the interaction of waves with the Juan Fernández Ridge (JFR). In Figure 3 we show the TR process for station juan to illustrate the interaction. The snapshots of tsunami waves are plotted in each panel, and the time is denoted by the simulation time, with $t = 12,000$ s being the last time step, i.e., the earthquake origin time and the final TR image. It is clear that, from $t = 9400$ s to $t = 9800$ s, the difference in water depth

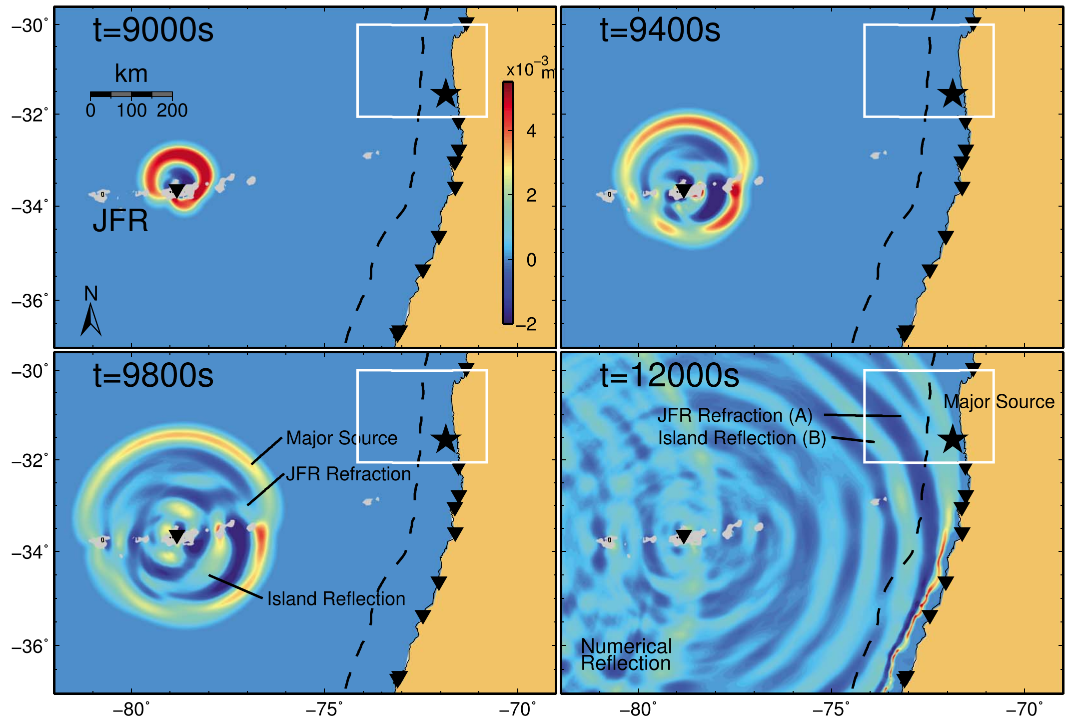

Figure 3. The TR process for station juan and wave interaction with JFR. The grey areas located roughly along latitude 34°S mark the JRF, where the water depth is much shallower than the surrounding ocean. The simulation starts at $t = 0$ s, but waves are not emitted from juan until the first crest shows up at about 9000 s. Waves refracted by JFR and reflected at the islands evolve to artifact A and B, respectively. Note that waves have bounced back from the computational boundaries at $t = 12,000$ s because of the wall boundary conditions adopted in the numerical simulation.

between JFR and the surrounding ocean causes wave refraction, which evolves to the closer artifact (artifact A). The farther artifact (artifact B) originates from the reflection of waves at the offshore islands. In this study, those artifacts are inevitable due to the limitation of stations. If more stations are available for TR analysis, the major source will be strengthened by wave interference, leading to relatively weaker artifacts.

The prediction of tsunami waves at all 24 stations from the final TR image is plotted in Figure S2 in the supporting information. The results show that the stations to the north of the epicenter have slightly earlier arrivals than observed, owing to the artificial lobe attached to the major source. Likewise, the artifacts to the southwest of the major source lead to an early phase at station juan. The overall matching of waveforms is satisfactory, and the key features of the waves, i.e., wave amplitude, period, and arrival time, are well reproduced at most stations.

In Figure 4 we compare the TR results with the initial sea surface deformation predicted by four published slip models and our joint model. We note here that the trench line shown in the figure is given by the PLATES project (http://www-udc.ig.utexas.edu/external/plates/data.htm), which is about 15 km to the east of that given by *Bird* [2003] that is used in some studies [*Melgar et al.*, 2016; *Heidarzadeh et al.*, 2016b]. Figure 4 shows that all the slip models locate the principal slip zone to the north of the epicenter, but the details of the slip distribution and the amount of near-trench slip vary from model to model, leading to different profiles of initial water elevation. The maximum initial water height also varies substantially from ∼1.4 m predicted by *Heidarzadeh et al.* [2016b] to ∼3.4 m by *Melgar et al.* [2016]. Among all the models, we find that our joint model predicts the most similar profile of initial deformation in comparison to the TR results, which is featured by a region of elevation that is oblique to the trench. The maximum water height from the TR results is about 2.0 m, located ∼30 km to the east of the trench, which also agrees well with our joint model. It is therefore indicated that the TR results are consistent with our joint model in which the maximum slip is located about 40–60 km to the east of the trench and the near-trench slip is relatively low (<3 m).

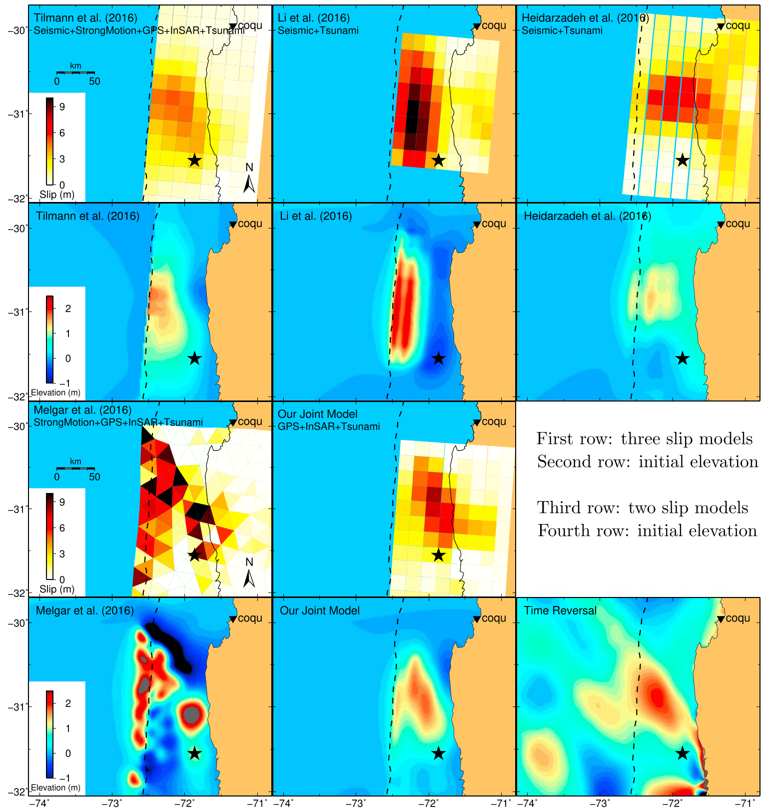

Figure 4. Comparison of the TR results with the initial elevation predicted by slip models. (first and third rows) The slip models, and (second and fourth rows) the corresponding initial water elevation. The black star marks the CSN epicenter, and the black dashed line denotes the trench. The color scale of slip and water height is the same for all the plots, respectively.

4. Discussion

In traditional acoustic TR experiments, the transducers are usually aligned along a straight line with small gaps that are less than a wavelength, which is referred to as time reversal mirror (TRM) [e.g., *Fink et al.*, 2000]. However, the actual distribution of the tsunami stations hardly satisfies the TRM condition due to uneven azimuthal coverage and large distance gaps between stations. In the case of 2011 Tohoku event, the tsunami waves were recorded by more than 50 sensors near Japan. Hence, the amount of data is adequate, and the azimuthal coverage of tsunami stations is also acceptable. However, in the 2015 Illapel event, although there are more than 20 tsunami stations, the azimuthal coverage of the stations is far from ideal. This raises the question if more data with similar azimuth can improve the TR imaging. In this study, we did not use all 24 tsunami stations but adopted data from only four stations at different azimuthal locations. This is because 20 stations out of the total 24 are aligned along the strike direction of the fault. Adopting all of them would lead to a focused source dominated by waves that propagate in the strike direction. As shown in Figure 5, the TR image obtained from all 24 stations is featured by an elongated area of water elevation in the east-west direction. Since most waves are propagating from north to south or from south to north in the TR process, they interfere in the southern region and constrain the northern and southern borders (top and bottom) relatively well. However, lacking data from the western side lead to large uncertainties in determining the western and eastern borders (left and right) of the tsunami source. In the supporting information, we plot the TR results of using 4–14 stations in Figure S6. It demonstrates that the final image is gradually dominated by the wave focusing in the east-west direction when the number of stations increases. This is consistent with the aforementioned results of 24 stations. In Figures S7 and S8, we show the TR image using one more DART station 32412 that is located at a relatively far distance from the source. The water elevation profile thus obtained is very similar to the result of four stations after normalized to the same maximum amplitude. In traditional acoustic experiments, it has been demonstrated that reflected waves can be used to image the source. For example, *Fink et al.* [2000] show that, in an enclosed cavity with reflecting boundaries, only one single

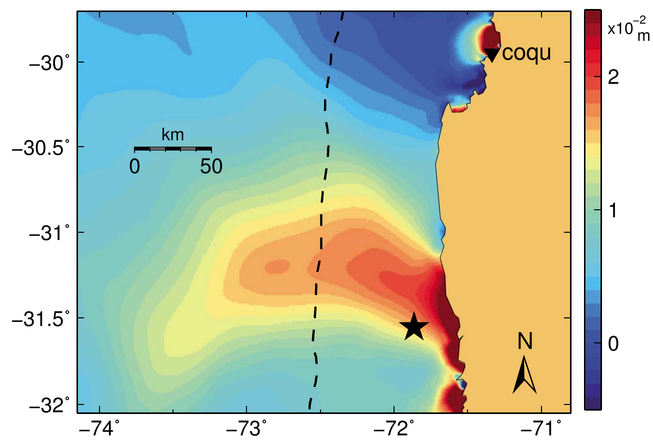

Figure 5. The TR image using all the 24 stations. The water elevation is distributed in an elongated area because most of the waves propagate in the along-strike direction during the TR process. Note that the absolute value of the water height is not scaled by the real tsunami data, so it is much smaller than that shown in Figure 2.

transducer is required to recover the source by time-reversing long enough records with reflected signals from the boundaries. *Hossen et al.* [2015a] proposed that reflected tsunami waves could also potentially help improving the tsunami source focusing. In Figure S9 we present the TR image using the complete waveforms of 12,000 s at the four selected stations. The results show more artifacts near the coastline than the results of using only the first crest. This could be attributed to inaccurate simulations of the reflected waves due to bathymetry uncertainties and neglecting of nonlinearity.

The TR results from all 24 stations also indicate the importance of station juan in constraining the border of the tsunami source perpendicular to the strike direction, since it is the only station located perpendicular to the strike direction. Other stations provide sufficient constraints on the northern and southern borders of the tsunami source, but they have little sensitivity on the western and eastern borders. juan is a tide gauge located near an offshore island, so the accuracy of simulating tsunami waves at the gauge largely depends on the resolution of the bathymetry data. If local bathymetry data with high resolution is available, it will clearly improve the estimation of the tsunami source. In addition, the final TR image is a static snapshot of the sea surface deformation, which ignores the kinematic rupture process of the earthquake. All the slip models shown in Figure 4 except our joint model are kinematic models, with earthquake source duration lasting about 100 s, causing uncertainties in estimating the location of the tsunami source. According to studies of seismic data [e.g., *Li et al.*, 2016], most energy was radiated between 20 s and 80 s from earthquake origin time, so we can use 60 s to estimate the propagation distance of tsunami waves during the earthquake rupture. Given that the water depth near the trench is around 6000 m, this leads to a tsunami speed of $\sqrt{gh} = 242.5$ m/s with h being the water depth. Thus, ignoring the kinematic rupture process of the earthquake will result in a maximum error of ∼14.5 km in our estimation of the location of the tsunami source.

5. Conclusion

In this study, we applied the TR technique to reconstruct the tsunami source of the 2015 Illapel earthquake. We introduced a correction to account for the 2-D spreading effects, which improved the TR results by isolating the tsunami source from the wave focusing along the coastline and reducing the artifacts. Results show that using four tsunami stations led to a satisfactory image of the tsunami source, albeit with two areas of artificial wave focusing resulting from wave interaction with the JFR. The tsunami source has an oblique profile to the strike direction and a maximum water height of ∼2.0 m located ∼30 km to the east of the trench. The final TR image is compared with the initial water elevation predicted by several published slip models, and it is highly consistent with our joint model that has a maximum slip of ∼8 m located about 40 ∼ 60 km to the east of the trench and relatively low near-trench slip (< 3 m).

Acknowledgments
This work made use of GMT software. The tsunami data at DART stations were downloaded from NOAA's website (http://www.ndbc.noaa.gov/dart.shtml); the tsunami data at tide gauges were downloaded from the IOC's website (http://www.ioc-sealevelmonitoring.org). The simulation of tsunami waves was carried out on supercomputer Stampede. This work is supported by the Hellman fellowship and the UCLA faculty research grant. We thank two anonymous reviewers for their valuable suggestions and comments which lead to further analysis and better formatting of the manuscript.

References

An, C., and P. L.-F. Liu (2014), Characteristics of leading tsunami waves generated in three recent tsunami events, *J. Earthquake Tsunami*, *8*(3), 1440001.

An, C., I. Sepúlveda, and P. L.-F. Liu (2014), Tsunami source and its validation of the 2014 Iquique, Chile, earthquake, *Geophys. Res. Lett.*, *41*, 3988–3994, doi:10.1002/2014GL060567.

Baba, T., R. Cummins, and T. Hori (2005), Compound fault rupture during the 2004 off the Kii Peninsula earthquake (M 7.4) inferred from highly resolved coseismic sea-surface deformation, *Earth Planets Space*, *57*(3), 167–172.

Bird, P. (2003), An updated digital model of plate boundaries, *Geochem. Geophys. Geosyst.*, *4*(3), 1027, doi:10.1029/2001GC000252.

Fink, M. (1992), Time reversal of ultrasonic fields. I. Basic principles, *IEEE Trans. Ultrason. Ferroelectr. Freq. Control*, *39*(5), 555–566.

Fink, M., D. Cassereau, A. Derode, C. Prada, P. Roux, M. Tanter, J.-L. Thomas, and F. Wu (2000), Time-reversed acoustics, *Rep. Prog. Phys.*, *63*(12), 1933.

Fuentes, M., S. Riquelme, G. Hayes, M. Medina, D. Melgar, G. Vargas, J. González, and A. Villalobos (2016), A study of the 2015 M_w 8.3 Illapel earthquake and tsunami: Numerical and analytical approaches, *Pure Appl. Geophys.*, *173*(6), 1847–1858.

Fujii, Y., K. Satake, S. Sakai, M. Shinohara, and T. Kanazawa (2011), Tsunami source of the 2011 off the Pacific coast of Tohoku earthquake, *Earth Planets Space*, *63*(7), 815–820.

Gusman, A. R., S. Murotani, K. Satake, M. Heidarzadeh, E. Gunawan, S. Watada, and B. Schurr (2015), Fault slip distribution of the 2014 Iquique, Chile, earthquake estimated from ocean-wide tsunami waveforms and GPS data, *Geophys. Res. Lett.*, *42*, 1053–1060, doi:10.1002/2014GL062604.

Heidarzadeh, M., T. Harada, K. Satake, T. Ishibe, and A. R. Gusman (2016a), Comparative study of two tsunamigenic earthquakes in the Solomon Islands: 2015 M_w 7.0 normal-fault and 2013 Santa Cruz M_w 8.0 megathrust earthquakes, *Geophys. Res. Lett.*, *43*, 4340–4349, doi:10.1002/2016GL068601.

Heidarzadeh, M., S. Murotani, K. Satake, T. Ishibe, and A. R. Gusman (2016b), Source model of the 16 September 2015 Illapel, Chile, M_w 8.4 earthquake based on teleseismic and tsunami data, *Geophys. Res. Lett.*, *43*, 643–650, doi:10.1002/2015GL067297.

Hossen, M. J., P. R. Cummins, S. G. Roberts, and S. Allgeyer (2015a), Time reversal imaging of the tsunami source, *Pure Appl. Geophys.*, *172*(3–4), 969–984.

Hossen, M. J., P. R. Cummins, J. Dettmer, and T. Baba (2015b), Time reverse imaging for far-field tsunami forecasting: 2011 Tohoku earthquake case study, *Geophys. Res. Lett.*, *42*, 9906–9915, doi:10.1002/2015GL065868.

Kajiura, K. (1963), The leading wave of a tsunami, *Bull. Earthquake Res. Inst. Univ. Tokyo*, *41*, 535–571.

Kanamori, H. (1972), Mechanism of tsunami earthquakes, *Phys. Earth Planet. Inter.*, *6*(5), 346–359.

Kawakatsu, H., and J.-P. Montagner (2008), Time-reversal seismic-source imaging and moment-tensor inversion, *Geophys. J. Int.*, *175*(2), 686–688.

Korolev, Y. P. (2011), An approximate method of short-term tsunami forecast and the hindcasting of some recent events, *Nat. Hazards Earth Syst. Sci.*, *11*(11), 3081–3091.

Larmat, C., J.-P. Montagner, M. Fink, Y. Capdeville, A. Tourin, and E. Clévédé (2006), Time-reversal imaging of seismic sources and application to the great Sumatra earthquake, *Geophys. Res. Lett.*, *33*, L19312, doi:10.1029/2006GL026336.

Lay, T., C. J. Ammon, H. Kanamori, L. Xue, and M. J. Kim (2011), Possible large near-trench slip during the 2011 M_w 9.0 off the Pacific coast of Tohoku earthquake, *Earth Planets Space*, *63*(7), 687–692.

Lay, T., H. Kanamori, C. J. Ammon, K. D. Koper, A. R. Hutko, L. Ye, H. Yue, and T. M. Rushing (2012), Depth-varying rupture properties of subduction zone megathrust faults, *J. Geophys. Res.*, *117*, B04311, doi:10.1029/2011JB009133.

Lay, T., H. Yue, E. E. Brodsky, and C. An (2014), The 1 April 2014 Iquique, Chile, M_w 8.1 earthquake rupture sequence, *Geophys. Res. Lett.*, *41*, 3818–3825, doi:10.1002/2014GL060238.

Li, L., T. Lay, K. F. Cheung, and L. Ye (2016), Joint modeling of teleseismic and tsunami wave observations to constrain the 16 September 2015 Illapel, Chile, M_w 8.3 earthquake rupture process, *Geophys. Res. Lett.*, *43*, 4303–4312, doi:10.1002/2016GL068674.

Liu, P., S. Woo, and Y. Cho (1998), Computer programs for tsunami propagation and inundation, *Tech. Rep.*, Cornell Univ., Ithaca, N. Y.

Ma, S. (2012), A self-consistent mechanism for slow dynamic deformation and tsunami generation for earthquakes in the shallow subduction zone, *Geophys. Res. Lett.*, *39*, L11310, doi:10.1029/2012GL051854.

Maeda, T., T. Furumura, S. Sakai, and M. Shinohara (2011), Significant tsunami observed at ocean-bottom pressure gauges during the 2011 off the Pacific coast of Tohoku earthquake, *Earth Planets Space*, *63*(7), 803–808.

Melgar, D., W. Fan, S. Riquelme, J. Geng, C. Liang, M. Fuentes, G. Vargas, R. M. Allen, P. M. Shearer, and E. J. Fielding (2016), Slip segmentation and slow rupture to the trench during the 2015, M_w8.3 Illapel, Chile earthquake, *Geophys. Res. Lett.*, *43*, 961–966, doi:10.1002/2015GL067369.

Okada, Y. (1985), Surface deformation due to shear and tensile faults in a half-space, *Bull. Seismol. Soc. Am.*, *75*(4), 1135–1154.

Satake, K. (1987), Inversion of tsunami waveforms for the estimation of a fault heterogeneity: Method and numerical experiments, *J. Phys. Earth*, *35*(3), 241–254.

Satake, K., Y. Fujii, T. Harada, and Y. Namegaya (2013), Time and space distribution of coseismic slip of the 2011 Tohoku earthquake as inferred from tsunami waveform data, *Bull. Seismol. Soc. Am.*, *103*(2B), 1473–1492.

Sato, M., T. Ishikawa, N. Ujihara, S. Yoshida, M. Fujita, M. Mochizuki, and A. Asada (2011), Displacement above the hypocenter of the 2011 Tohoku-Oki earthquake, *Science*, *332*(6036), 1395–1395.

Shao, G., X. Li, C. Ji, and T. Maeda (2011), Focal mechanism and slip history of the 2011 M_w 9.1 off the Pacific coast of Tohoku earthquake, constrained with teleseismic body and surface waves, *Earth Planets Space*, *63*(7), 559–564.

Shuto, N. (1991), Numerical simulation of tsunamis—Its present and near future, *Nat. Hazards*, *4*(2–3), 171–191.

Tanter, M., J.-L. Thomas, and M. Fink (2000), Time reversal and the inverse filter, *J. Acoust. Soc. Am.*, *108*(1), 223–234.

Tilmann, F., et al. (2016), The 2015 Illapel earthquake, central Chile: A type case for a characteristic earthquake?, *Geophys. Res. Lett.*, *43*, 574–583, doi:10.1002/2015GL066963.

Tsushima, H., K. Hirata, Y. Hayashi, Y. Tanioka, K. Kimura, S. Sakai, M. Shinohara, T. Kanazawa, R. Hino, and K. Maeda (2011), Near-field tsunami forecasting using offshore tsunami data from the 2011 off the Pacific coast of Tohoku earthquake, *Earth Planets Space*, *63*(7), 821–826.

Tsushima, H., R. Hino, Y. Ohta, T. Iinuma, and S. Miura (2014), tFISH/RAPiD: Rapid improvement of near-field tsunami forecasting based on offshore tsunami data by incorporating onshore GNSS data, *Geophys. Res. Lett.*, *41*, 3390–3397, doi:10.1002/2014GL059863.

Wang, X., and P. L.-F. Liu (2006), An analysis of 2004 Sumatra earthquake fault plane mechanisms and Indian Ocean tsunami, *J. Hydraul. Res.*, *44*(2), 147–154.

Wang, X., and P. L.-F. Liu (2007), Numerical simulations of the 2004 Indian Ocean tsunamis—Coastal effects, *J. Earthquake Tsunami*, *1*(3), 273–297.

Wei, Y., C. Chamberlin, V. V. Titov, L. Tang, and E. N. Bernard (2013), Modeling of the 2011 Japan tsunami: Lessons for near-field forecast, *Pure Appl. Geophys.*, *170*(6–8), 1309–1331.

Yagi, Y., R. Okuwaki, B. Enescu, S. Hirano, Y. Yamagami, S. Endo, and T. Komoro (2014), Rupture process of the 2014 Iquique Chile earthquake in relation with the foreshock activity, *Geophys. Res. Lett.*, *41*, 4201–4206, doi:10.1002/2014GL060274.

Yue, H., and T. Lay (2011), Inversion of high-rate (1 sps) GPS data for rupture process of the 11 March 2011 Tohoku earthquake (M_w 9.1), *Geophys. Res. Lett.*, *38*, L00G09, doi:10.1029/2011GL048700.

Yue, H., T. Lay, L. Rivera, Y. Bai, Y. Yamazaki, K. F. Cheung, E. M. Hill, K. Sieh, W. Kongko, and A. Muhari (2014), Rupture process of the 2010 M_w 7.8 Mentawai tsunami earthquake from joint inversion of near-field hr-GPS and teleseismic body wave recordings constrained by tsunami observations, *J. Geophys. Res. Solid Earth*, *119*, 5574–5593, doi:10.1002/2014JB011082.